Nanoscale

Accepted Manuscript

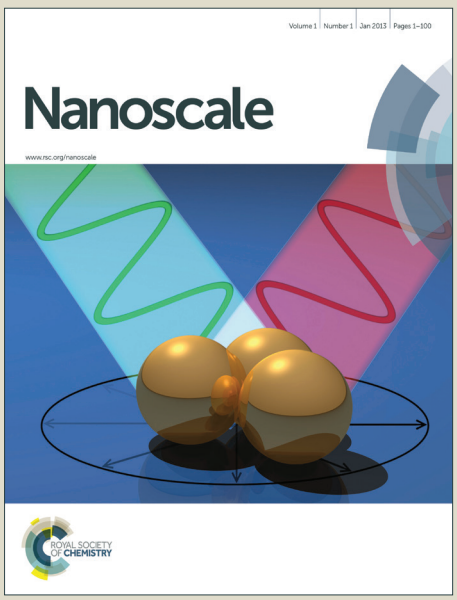

ROYAL SOCIETY OF CHEMISTRY

www.rsc.org/nanoscale

Nanoscale

RSCPublishing

PAPER

Incorporation of a self-aligned selective emitter to realize highly efficient (12.8%) Si nanowire solar cells

Cite this: DOI: 10.1039/xoxxoooooox

Han-Don Um,[a,†] Kwang-Tae Park,[a,†] Jin-Young Jung,[a] Xiaopeng Li,[b,c] Keya Zhou,[a] Sang-Won Jee[a] and Jung-Ho Lee*[a]

Received ooth January 2012,
Accepted ooth January 2012

DOI: 10.1039/xoxxoooooox

www.rsc.org/

Formation of a selective emitter in crystalline silicon solar cells improves photovoltaic conversion efficiency by decoupling emitter regions for light absorption (moderately doped) and metallization (degenerately doped). However, use of a selective emitter in silicon nanowire (Si NW) solar cells is technologically challenging because of difficulties in forming robust Ohmic contacts that interface directly with the top-ends of nanowires. Here we describe a self-aligned selective emitter successfully integrated into an antireflective Si NW solar cell. By one-step metal-assisted chemical etching, NW arrays formed only at light-absorbing areas between top-metal grids while selectively retaining Ohmic contact regions underneath the metal grids. We observed a remarkable ~40% enhancement in blue responses of internal quantum efficiency, corresponding to a conversion efficiency of 12.8% in comparison to the 8.05% of a conventional NW solar cell.

Introduction

Silicon nanowires (Si NWs) are considered candidates for next-generation solar cells because of their strong broadband optical absorptance despite reduced silicon usage.[1-17] However, the experimental conversion efficiencies reported to date for Si wire solar cells are much lower than the estimated theoretical efficiency.[16] One major hurdle is difficulty in forming a robust, Ohmic front electrode directly over the wire arrays. Non-Ohmic contacts formed between top-electrodes and a wire array increase series resistance while decreasing the fill factor (*FF*).[5, 15] In addition, a high surface-to-volume ratio of NWs increases the doping concentration (N_d) inside the NWs during thermal doping, so that the degenerately-doped NW emitter acts as a metal-like conductive layer, causing high Auger and Shockley-Read-Hall (SRH) recombination loss. As a result, the open-circuit voltage (V_{oc}) decreases due to increased surface recombination of charge carriers,[18] and the short-circuit current density (J_{sc}) is also depressed due to degraded blue responses by loss of high-energy photons.

Integration of selective-emitter technology into Si NW solar cells can improve cell efficiency by decoupling the degenerately-doped (10^{20}–10^{21}/cm^3) contact region from the lightly-doped (10^{18}–10^{19}/cm^3) emitter region for photon collection.[19] Reduced recombination by a lightly-doped emitter results in higher V_{oc} and J_{sc} values and lowers the collection losses of photogenerated carriers. Although the conventional selective-emitter process in crystalline Si solar cells requires multiple doping steps with photomask alignments,[20-22] we developed a facile etch-back approach to integrate a self-aligned selective emitter onto a degenerately doped, Si NW solar cell. Robust Ohmic contacts integrated with lightly-doped antireflective Si NWs were obtained using one-step thermal diffusion. Our selective-emitter-NW solar cell had a conversion efficiency of 12.8% due to the low contact resistance of 3.03 mΩ·cm^2 as well as a high J_{sc} value of 33.65 mA/cm^2. In particular, blue responses showed a remarkable enhancement of ~40% due to improvement of internal quantum efficiency (IQE), indicating efficient collection of charge carriers photogenerated in the NWs. In addition, the considerable enhancement in IQE over broadband wavelengths implies that superior light trapping by Si NWs combined synergistically with efficient carrier collection by the selective-emitter structure.

Results and discussion

The essential features required to fabricate selective-emitter NW solar cells are illustrated in Fig. 1. We used one-step metal-assisted chemical etching (MACE) to form moderately doped NWs at the low-doped bottom side of a planar n-doped emitter, while removing degenerately-doped, top-ends of the original NWs. Self-aligned, degenerately doped regions remained underneath the metal grids for formation of Ohmic contacts. Phosphorus doping was then performed using a spin-on-doping technique to form p-n junctions. The depth of the p-n junctions was estimated to be ~0.6 μm from the surface, and the surface dopant concentration was measured to be ~10^{21}/cm^3 based on the secondary ion mass spectrometry (SIMS) profile plotted in Fig. 1a. Front metal grids of Ti and Au were prepared simply using a mask evaporation technique. After metallization, antireflective Si NWs were prepared using MACE on emitter regions exposed between metal grids. As shown in Fig. 1b, one-step MACE yielded a selective-emitter structure consisting of lightly-doped NWs and Ohmic contacts, because the degenerately-doped top-ends of NWs positioned in-between the metal grids were selectively removed during MACE.

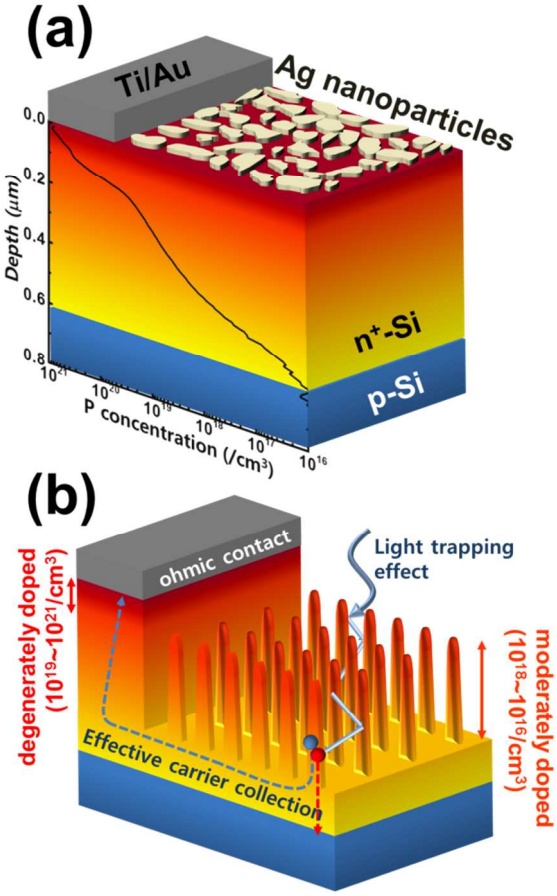

Fig. 1 Schematic showing the key features of self-aligned selective-emitter-NW solar cells. (a) Ag NPs are deposited onto a planar solar cell by a galvanic displacement process. A SIMS depth profile of phosphorous overlaps with p-n junctions. (b) MACE results in the formation of moderately-doped Si NWs at the light absorbing area while leaving metal electrodes on top of the degenerately doped Si.

According to the localized galvanic cell model,[23,24] the MACE mechanism involves a microscopic electrochemical process in which Ag nanoparticles (Ag NPs) as a catalyst promote a cathodic reaction (reduction of H_2O_2) as well as an anodic reaction (oxidation of Si). In aqueous H_2O_2/HF solution, local oxidation of Si occurs underneath the Ag NPs; then, the oxidized Si is dissolved by HF (Reaction 1 in Fig. 2a). With increasing etching time, Si can adopt a wirelike morphology because of further penetration of Ag NPs into the Si bulk. Meanwhile, Ag^+ ions can be created by the oxidation of Ag NPs by H_2O_2 at the interface between Si and the Ag NPs (Reaction 2):[25, 26]

$$2Ag + H_2O_2 + 2H^+ \rightarrow 2Ag^+ + 2H_2O \quad \text{(Reaction 2)}$$

$$Si + 4Ag^+ + 6F^- \rightarrow 4Ag + SiF_6^{2-} \quad \text{(Reaction 3)}$$

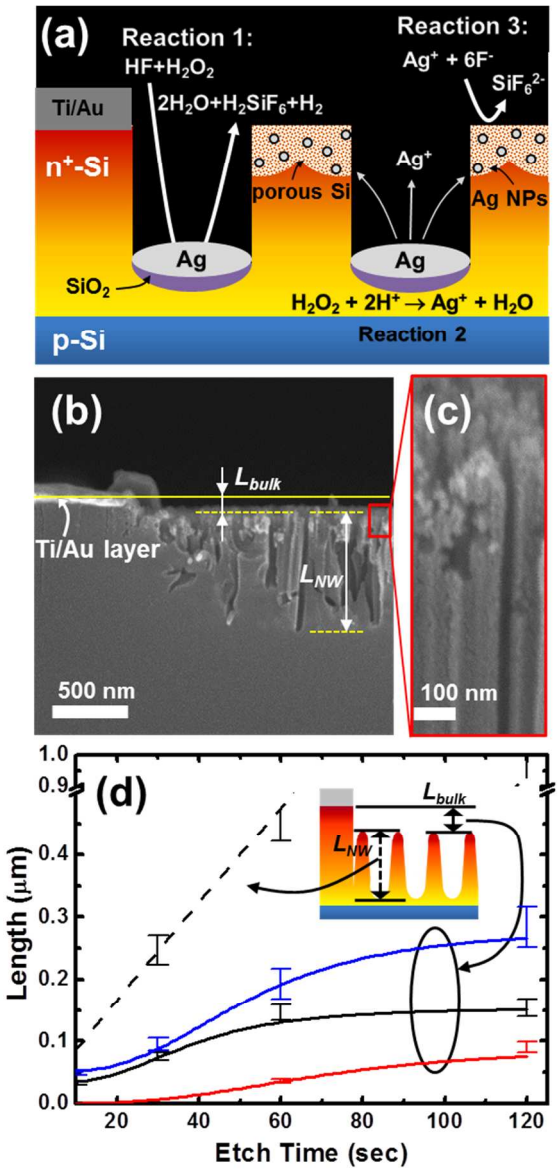

Fig. 2 (a) Schematic describing the reaction steps for the formation of moderately-doped Si NWs. (b) Cross-sectional SEM image of Si NWs selectively etched at the light absorbing area. The solid yellow line indicates the interface between the metal layer and silicon. (c) Magnified view showing the rough and porous morphology around the NW tips. (d) Lengths of selective-emitter-NWs (L_{NW}, dotted line) and bulk Si etching (L_{bulk}, solid lines) are plotted as a function of etch time, for H_2O_2 concentrations [H_2O_2] of 0. 015 (red), 0.045 (black), and 0.18 (blue) M.

These Ag^+ ions are normally reduced back to Ag NPs by attracting electrons, because the Si-adherent Ag NPs have a higher electronegativity than Si.[27] Ag^+ ions are likely confined in close proximity to Ag NPs, resulting in the presence of Ag NPs confined to the original sites. To etch degenerately-doped Si, however, some of the Ag^+ ions are able to preferentially nucleate tiny Ag NPs onto defective sites where the energy barrier for redox reactions is lower, rather than being confined to the original sites of Ag NPs. This feature was revealed by the presence of tiny Ag NPs creating new lateral etching pathways,

which increased surface roughness and porosity as well (reaction 3).[28] As a result, the heavily doped, top-regions of NWs become morphologically rough and porous (Fig. 2b and 2c, Supplementary information Fig. S1). Highly porous Si around the NW tips could be quickly removed by H_2O_2/HF solution, leading to an empty space (L_{bulk}) at the light absorption region shown in Fig. 2b.

Fig. 2d shows how the NW length (L_{NW}) of the selective emitter and bulk Si etching (L_{bulk}) can be controlled as a function of etch time in various H_2O_2 concentrations. MACE can be used to obtain selective-emitter NWs while removing degenerately doped regions. NW length increased linearly with etch time (dotted line); however, L_{bulk} in 0.045 M H_2O_2 solution was normally saturated at the depth of ~150 nm (black line), which was degenerately doped with $\geq 5\times10^{19}$/cm^3 of P. We adjusted the amount of bulk Si etching by varying the H_2O_2 concentration in the HF/H_2O_2 solution. A high H_2O_2 concentration (i.e., 0.18 M, blue line) resulted in the generation of more Ag^+ ions and tiny Ag NPs due to oxidation of Ag such that the extent of porous Si and bulk Si etching was higher in the relatively low-doped Si sample than that obtained using a lower H_2O_2 concentration (0. 015M, red line). As a result, L_{bulk} increased with increasing H_2O_2 concentration, as shown in Fig. 2d.

The reflectance (R_{avg} in the inset of Fig. 3a), wavelength-averaged over the main spectral range from 400 to 1000 nm, decreased from ~38.5% to ~2.7% with increasing etch time up to 2 min. This superior anti-reflectance originated mainly from improved matching of the optical impedance of air and bulk Si due to the presence of Si NWs.[12] Enhanced light absorptance increased J_{sc} in selective-emitter-NW cells (J–V curves in Fig. 3a); however, the best cell was obtained from the sample which has been etched for 1 minute only, not from the 2-min-etched cell that had the highest light absorptance (lowest R_{avg}). We recorded a photovoltaic conversion efficiency of 12.89% for our best cell, along with V_{oc}, J_{sc}, and FF values of 555 mV, 33.65 mA/cm^2, and 68.6%, respectively. V_{oc} and FF values initially tended to increase with etch time up to 0.5 min, but then decreased (1–2 min). Improved V_{oc} was due to suppression of Auger recombination by removal of degenerately-doped Si, despite the increase in surface recombination and surface area for 0.5-min etching. Increasing the etching time to longer than 0.5 min, however, decreased V_{oc} because surface recombination aggravated by longer NWs governed device performance. Reverse saturation current density (J_0) extracted from the illuminated J–V curves[29] is plotted in Fig. 3b. The 0.5-min-etched cell had the lowest J_0 value (highest V_{oc}), implying an optimized recombination state by the following relations between J_0 and V_{oc}:

$$V_{oc} = \frac{k_b T}{q} \ln\left(\frac{J_L}{J_0} + 1\right)$$

where q, k_B, T, and J_L represent electron charge, Boltzmann's constant, temperature, and light-generated current, respectively. FF values also decreased with increasing NW length (i.e., increasing etch time, Fig. 3c) because the doping concentration inside the longer NWs further decreased such that series and emitter sheet resistances all increased.

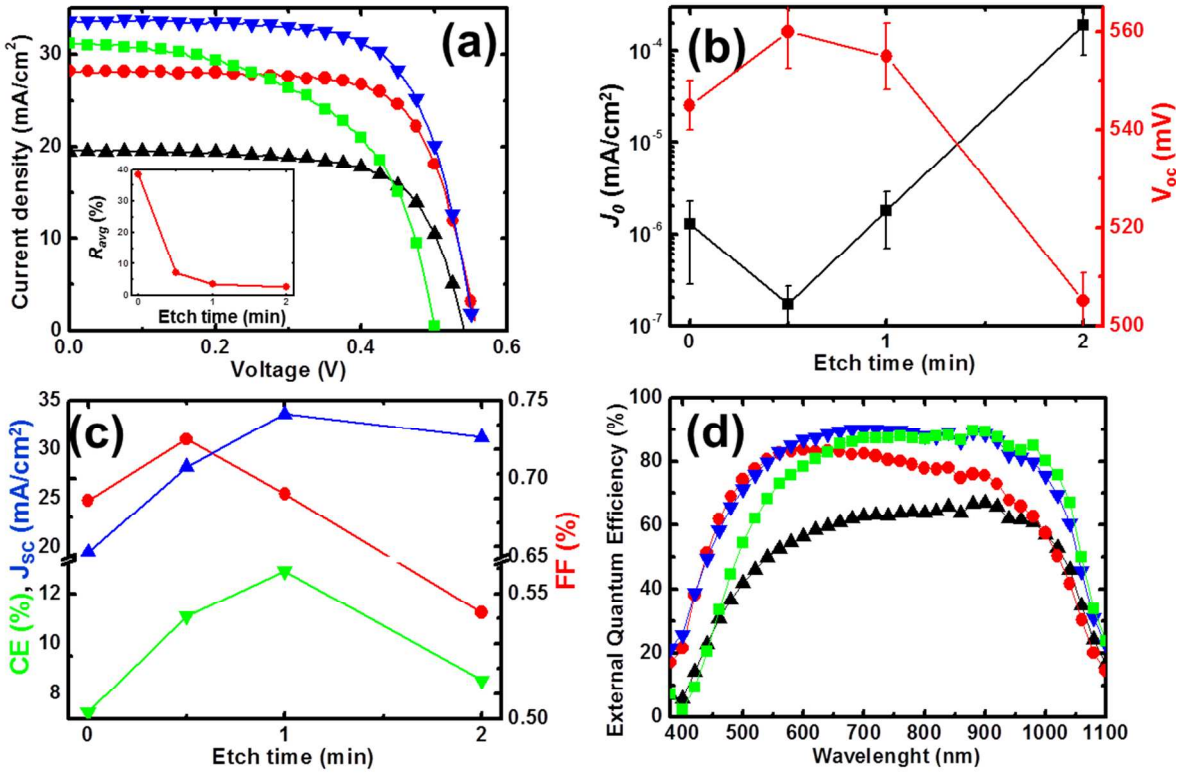

Fig. 3 (a) J–V curves of selective-emitter-NW solar cells with different etch times; 0 (black), 0.5 (red), 1 (blue) and 2 (green) min. Inset shows the average reflectance (R_{ave}), which is spectrally weighted over the wavelengths of 400~1000 nm. (b) Reverse saturation current density (J_0, black) and open-circuit voltage (V_{oc}, red) extracted from the J–V curves plotted in panel a. (c) J_{sc} (blue), FF (red), and the conversion efficiency (green) of selective-emitter-NW solar cells are plotted as a function of etch time. (d) EQEs with different etch times; 0 (black), 0.5 (red), 1 (blue) and 2 (green) min.

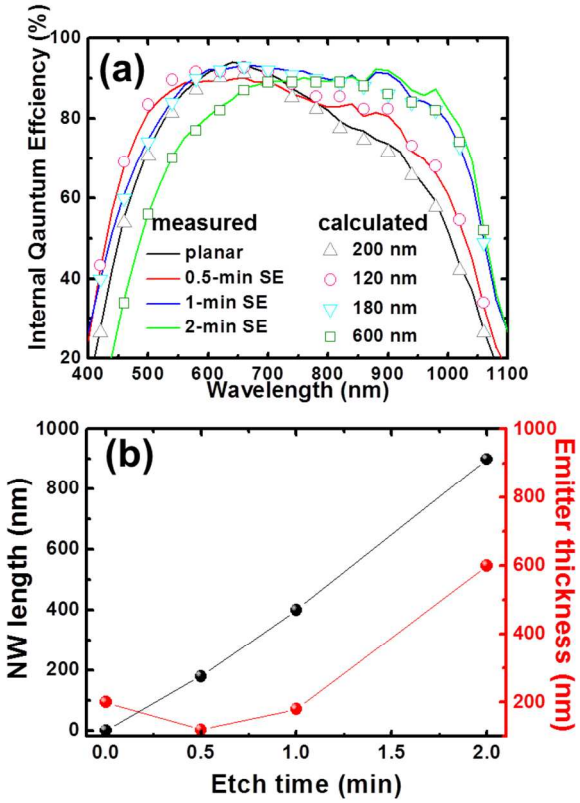

Fig. 4 (a) IQEs of planar and selective-emitter-NW solar cells. All symbols are PC1D-calculated IQEs, which best fit the measured IQEs. The etch time (measured) was converted to the thickness of the degenerately P-doped emitter for the calculated symbols. (b) Lengths of NWs (measured, black) are compared with the emitter thicknesses (calculated, red) of panel a, extracted from the PC1D simulation.

The typical series resistances of standard solar cells is ~2 Ωcm^2 [30]; in contrast, that of the 2-min-etched cell was ~4.8 Ωcm^2. As a result, *FF* values decreased from 72 to 53% with increasing etch time from 0.5 to 2 min. Although excellent V_{oc} and *FF* values were obtained for the 0.5-min etched cell, the best conversion efficiency was recorded for the 1-min etched cell, which had the highest J_{sc} value.

Increased light absorptance with etch time was consistent with the increase in J_{sc} values; however, the improvement in J_{sc} appeared to be limited to an etch time of 1 min. External quantum efficiencies (EQEs, Fig. 3d) of short-wavelengths (400–550 nm) indicated that the blue responses (high-energy photons) of the 0.5- and 1-min cells improved relative to the planar counterpart because of decreased Auger recombination as well as increased light absorptance. Without surface passivation, however, the remarkable increase in NW length (2-min etched) diminished the EQEs of high-energy photons by surface recombination. In contrast, the improvement in quantum efficiency of low-energy photons (long wavelengths) was directly proportional to the NW length, because longer NWs are more effective at trapping light.[6] The measured J_{sc} values in Fig. 3c can also be estimated from EQE spectra by using the following equation:

$$J_{sc} = \frac{q}{hc} \times \int S_s Q_x \lambda d\lambda$$

where S_s is the AM 1.5G solar spectrum, Q_x is EQE, λ is a light wavelength, q is the electron charge, h is Planck's constant, and c is the speed of light. The highest J_{sc} value (33.65 mA/cm^2) was obtained under optimized conditions (1-min etched) for carrier collections for both short and long wavelengths, despite the superior antireflectance properties of the 2-min etched cell.

Fig. 4a shows the measured and simulated IQEs for planar and selective-emitter NW solar cells. Simulated values were calculated from the optimized model using a commercially available, one-dimensional solar cell modeling program (PC1D) for IBM PC operation. Because PC1D was unable to model the NW morphology, the best fits for modeling IQE were extracted from thickness variations of degenerately P-doped (≥10^{19} cm^{-3}) emitters on planar cells, which optimizes Auger recombination to match the experimental data.[18] Our planar solar cell was optimized with the fitting results assuming an emitter thickness of 200 nm (Fig. 4b). Employing selective-emitter NWs improved IQE improvements (up to 1-min etch times) by decreased emitter thicknesses (decreasing Auger recombination) in comparison to the planar reference cell without NWs. Note that we optimized the emitter thicknesses in all NW samples to be thinner than the corresponding NW lengths. This clearly implies that certain portions of the NWs functioned as semiconductor (not metallic) light absorbers.

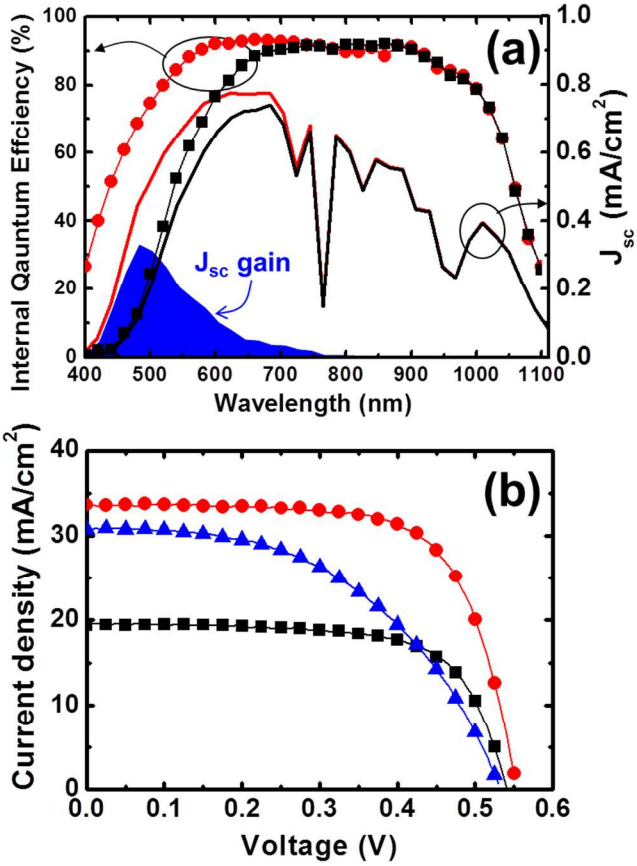

Fig. 5 (a) IQE vs. J_{sc} for the selective-emitter-NW (red) and conventional NW (black) solar cells. Blue area denotes the additional J_{sc} gained by adopting selective-emitter NWs. (b) *J*–*V* curves for planar (black), selective-emitter-NW (red), and conventional NW (blue) solar cells.

Fig. 5 compares the measured IQEs and current densities of conventional and selective-emitter-NW solar cells, in which the top-metal electrodes of the conventional NW solar cells directly contacted the NW tips after heavy doping of NWs. The blue response of the IQE spectra improved notably upon applying the selective-emitter NW structure, implying that Auger recombination due to degenerately doped emitters governed the IQE characteristics of high-energy photons. Severe degradation in the blue response of IQE is a typical characteristic of nanostructured solar cells with a high surface-to-volume ratio.[31] In most cases, poor J_{sc} and conversion efficiency have been reported to stem from surface recombination due to the large surface areas of nanostructures; however, in our work, we showed a clear difference between conventional and selective-emitter NWs, and demonstrated that increased recombination was mostly due to Auger recombination associated with nanostructured emitters that were more heavily doped than planar-emitters under identical thermal doping conditions. Despite their large surface areas, the blue response of IQE for selective-emitter-NWs increased from 7.0 to 60.8% at 450 nm, and reached >90% from 580 to 840 nm by simply decreasing the phosphorus concentrations. A significant J_{sc} gain was also obtained by employing a selective-emitter-NW structure. We obtained a J_{sc} value of ~3 mA/cm^2 for the selective-emitter solar cells, which is ≥10% higher than the value obtained for a conventional NW solar cell.

The conversion efficiency increased from 8 to 12.8% along with the improved J_{sc}, V_{oc}, and *FF* results (Table 1). In particular, *FF* was improved notably (68.6%) compared to conventional NW solar cells (49.4%) requiring direct Ohmic contacts using the NW tips. To extract contact resistivity (ρ_c), we applied the transmission line model (TLM)[32] which is a classical approach for determining contact resistance (R_c). To measure the R_c of Si/Ag, several metal grids were deposited on the Si surface in various samples. (Supplementary information Fig. S3). We can assume that the total resistance between any two metal grids is the sum of resistances of the two grid contacts ($2 \times R_c$) and silicon. The resistances were measured by adjusting the number of pitches between two metal grids, as shown in Fig. 6. At the *zero-point* (the intersection with the y-axis in Fig. 6) of the grid pitches, resistance was due to the two grid contacts ($2 \times R_c$) without the influence of the emitter, because the electric current only flowed through two contacts. In our work, the ρ_c (contact area × R_c) of Si/Ag in the selective-emitter NW structure was 3.03 mΩ cm^2 since the measured R_c was 0.91 Ω at the 3.30×10^{-3} cm^2 contact area. Owing to the formation of planar Ohmic contacts for the selective-emitter NW structure, a superior contact resistivity of 3.03 mΩ cm^2 was obtained in contrast to the value (25.90 mΩ cm^2) for conventional NW solar cells (Fig. 6). In practice, the *FF* value of selective-emitter NW solar cells was almost identical to that (69.3%) of a planar solar cell.

Table 1. Photovoltaic performances of planar, selective-emitter-NW, and conventional NW solar cells.

	V_{oc} [mV]	J_{sc} [mA/cm^2]	*FF* [%]	CE [%]
Planar cell	540	19.46	69.3	7.28
Conventional NW cell	531	30.73	49.4	8.05
Selective-emitter-NW cell	555	33.65	68.6	12.8

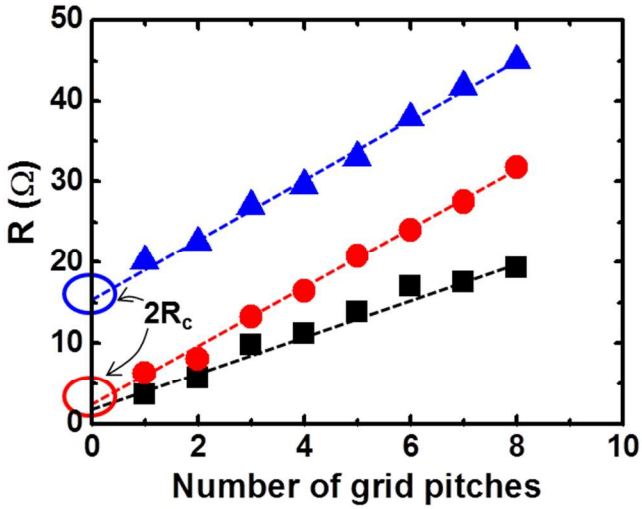

Fig. 6 Plot of resistances measured by varying the pitches of the grid lines; planar (black), selective-emitter-NW (red), and conventional NW (blue) solar cells.

Conclusions

In summary, we developed highly efficient (12.8%) nanowire solar cells by employing a *self-aligned* selective emitter structure without costly optical patterning. Using facile one-step etching, we obtained direct contacts between top-metal electrodes and degenerately-doped planar silicon, while concomitantly utilizing low-doped silicon nanowires as optical absorbers. This resulted in improvement of all photovoltaic parameters (V_{oc}, J_{sc}, and *FF*) in addition to a remarkable improvement (7.0 to 60.8% at 450 nm) in the blue response in the IQE. Our selective-emitter technique can be used to generate improved nanowire solar cells with superior light absorptance (improved carrier generation) as well as robust top-metal contacts (improved carrier collection).

Experimental Section

We used one-step metal-assisted chemical etching (MACE) to retain moderately doped NWs in the light absorption region by removing the top-ends (degenerately-doped) of the original NWs. We used 525-μm-thick, Czochralski-grown, 1–10 Ω·cm, p-Si(100) wafers. After standard RCA (Radio Corporation of America) cleaning, the emitter layer was formed by phosphorus diffusion adopting a spin-on-dopant (SOD) method, as described elsewhere.[11] Phosphorous silicate precursors (P509, Filmtronics) were spun onto a wafer, and n^{++}-emitter formed in a tube furnace using mixed ambient of N_2 and O_2 via thermal diffusion of gaseous phosphorous at 900°C for 30 min. Phosphorus glass that remained after SOD diffusion was removed using a diluted HF solution. Al was thermally evaporated for the backside electrode. Front metal grids of Ti and Au were prepared simply using a mask evaporation technique without the need for costly lithographic patterning; Ti and Au were evaporated onto the n^{++}-emitter layer via a shadow mask set (Fig. 1a). This patterning approach spontaneously generated metal-line patterns by metal deposition only without

the assistance of optical steppers, photoresists, or plasma etchers. The patterned structure of the front metal grids consisted of busbars with a width (w) of 500 μm and eight fingers (w=80 μm) arrayed perpendicularly to each busbar. These metal grids normally shaded ~9.95% of the total front-surface-area in our solar cells. Anti-reflective Si NWs were prepared using MACE applied only to emitter regions exposed between the metal grids. Silver nanoparticles (NPs) were precipitated uniformly for 10 s using a galvanic displacement reaction employing an aqueous solution of HF (4.8 M) and $AgNO_3$ (0.01M). After cleaning, Si NWs were allowed to form at room temperature for 10–120 s using a mixed solution of HF (4.8 M) and H_2O_2 (0.5 M). NW diameters were 50–200 nm and NW length was adjusted by varying the etch time. Residual Ag NPs were then removed using concentrated nitric acid (30 wt%) for 20 min, and the NWs were finally rinsed with de-ionized water. As shown in Fig. 1b, one-step MACE yielded a selective-emitter structure consisting of lightly-doped NWs and Ohmic contacts, because the degenerately-doped top-ends of NWs positioned in-between the metal grids were selectively removed during MACE. A sample area of 10×10 mm^2 was used for photovoltaic measurements of Si NW solar cells.

The depth profile of phosphorus ions has been measured by magnetic-sector secondary ion mass spectrometer (SIMS, CAMECA IMS 7f) attached with a Cs ionization source. The Cs^+ primary ions were accelerated to 10 keV, and the secondary positive ions were extracted at 5 keV. The surface morphology of Si NW arrays was characterized by Field-emission scanning electron microscopy (FE-SEM, Hitachi S-4800) and Field-emission transmission electron microscopy (FE-TEM, JEOL JEM-2100F). Optical reflection measurements were performed over wavelengths of 300–1000 nm using a UV–Vis/NIR spectrophotometer (Lambda 750, Perkin Elmer) equipped with a 60 mm integrating sphere (Labsphere) to account for total light (diffuse and specular) reflected from the samples. Photovoltaic properties of Si NW solar cells were investigated using a solar simulator (Peccel technology PEC-L11) as well as a potentiostat (HS-technologies Ivium stat) under 1-sun light intensity (100 mW cm^{-2}). A 150 W Xe arc lamp with AM 1.5 G filters was used as the light source. Incident flux was measured using a calibrated power meter, and double-checked using a NREL-calibrated solar cell (PV Measurements, Inc.). IQE was measured using a Xe light source and a monochromator at wavelengths of 400–1100 nm.

Acknowledgements

This work was supported by grants from the New & Renewable Energy Technology Development Program (No. 2009T100100614) and Human Resources Development (No. 20104010100620) of the Korea Institute of Energy Technology Evaluation and Planning (KETEP) funded by the Korea government Ministry of Knowledge Economy. This work was also supported by a grant from the National Research Foundation of Korea (NRF) funded by the Korea government (MEST) (No. 2011-0028604).

Notes and references

[a]Department of Materials and Chemical Engineering, Hanyang University, Ansan, 426-791, Korea. *E-mail: jungho@hanyang.ac.kr

[b]Max-Plank Institute of Microstructure Physics, Weinberg 2, 06120 Halle, Germany.

[c]Fraunhofer Institute for Mechanics of Materials, Walter-Hülse-Str. 1, 06120 Halle, Germany.

[†]These authors contributed equally to this work.

Electronic Supplementary Information (ESI) available: See DOI: 10.1039/b000000x/

1. B. M. Kayes, H. A. Atwater and N. S. Lewis, *J. Appl. Phys.*, 2005, **97**, 114302.
2. L. Tsakalakos, J. Balch, J. Fronheiser, B. A. Korevaar, O. Sulima and J. Rand, *Appl. Phys. Lett.*, 2007, **91**, 233117.
3. B. Z. Tian, X. L. Zheng, T. J. Kempa, Y. Fang, N. F. Yu, G. H. Yu, J. L. Huang and C. M. Lieber, *Nature*, 2007, **449**, 885-U888.
4. E. C. Garnett and P. D. Yang, *J. Am. Chem. Soc.*, 2008, **130**, 9224-9225.
5. O. Gunawan and S. Guha, *Sol. Energy Mater. Sol. Cells*, 2009, **93**, 1388-1393.
6. E. C. Garnett and P. D. Yang, *Nano Lett.*, 2010, **10**, 1082-1087.
7. H. P. Yoon, Y. A. Yuwen, C. E. Kendrick, G. D. Barber, N. J. Podraza, J. M. Redwing, T. E. Mallouk, C. R. Wronski and T. S. Mayer, *Appl. Phys. Lett.*, 2010, **96**, 213503.
8. Y. R. Lu and A. Lal, *Nano Lett.*, 2010, **10**, 4651-4656.
9. M. C. Putnam, S. W. Boettcher, M. D. Kelzenberg, D. B. Turner-Evans, J. M. Spurgeon, E. L. Warren, R. M. Briggs, N. S. Lewis and H. A. Atwater, *Energ Environ Sci*, 2010, **3**, 1037-1041.
10. H. D. Um, J. Y. Jung, H. S. Seo, K. T. Park, S. W. Jee, S. A. Moiz and J. H. Lee, *Jpn. J. Appl. Phys.*, 2010, **49**, 04DN02.
11. J. Y. Jung, Z. Guo, S. W. Jee, H. D. Um, K. T. Park, M. S. Hyun, J. M. Yang and J. H. Lee, *Nanotechnology*, 2010, **21**, 445303.
12. J. Y. Jung, Z. Guo, S. W. Jee, H. D. Um, K. T. Park and J. H. Lee, *Opt. Express*, 2010, **18**, A286-A292.
13. K. T. Park, Z. Guo, H. D. Um, J. Y. Jung, J. M. Yang, S. K. Lim, Y. S. Kim and J. H. Lee, *Opt. Express*, 2011, **19**, A41-A50.
14. D. Kumar, S. K. Srivastava, P. K. Singh, M. Husain and V. Kumar, *Sol. Energy Mater. Sol. Cells*, 2011, **95**, 215-218.
15. O. Gunawan, K. Wang, B. Fallahazad, Y. Zhang, E. Tutuc and S. Guha, *Prog. Photovoltaics*, 2011, **19**, 307-312.
16. M. D. Kelzenberg, D. B. Turner-Evans, M. C. Putnam, S. W. Boettcher, R. M. Briggs, J. Y. Baek, N. S. Lewis and H. A. Atwater, *Energ Environ Sci*, 2011, **4**, 866-871.
17. D. R. Kim, C. H. Lee, P. M. Rao, I. S. Cho and X. L. Zheng, *Nano Lett.*, 2011, **11**, 2704-2708.
18. H. C. Yuan, V. E. Yost, M. R. Page, P. Stradins, D. L. Meier and H. M. Branz, *Appl. Phys. Lett.*, 2009, **95**, 123501.
19. K. Misiakos and F. A. Lindholm, *Sol. Cells*, 1986, **17**, 29-52.
20. A. W. Blakers, A. Wang, A. M. Milne, J. H. Zhao and M. A. Green, *Appl. Phys. Lett.*, 1989, **55**, 1363-1365.
21. B. Paviet-Salomon, S. Gall, S. Manuel, R. Monna and A. Slaoui, Laser Doped Emitter Silicon Solar Cells, Valencia, Spain (WIP, Munich), 2010.
22. J. H. Zhao, A. H. Wang, M. A. Green and F. Ferrazza, *Appl. Phys. Lett.*, 1998, **73**, 1991-1993.
23. K. Peng, Y. Wu, H. Fang, X. Zhong, Y. Xu and J. Zhu, *Angew. Chem.-Int. Edit.*, 2005, **44**, 2737-2742.
24. M. L. Zhang, K. Q. Peng, X. Fan, J. S. Jie, R. Q. Zhang, S. T. Lee and N. B. Wong, *J. Phys. Chem. C*, 2008, **112**, 4444-4450.
25. S. Jana, S. Mondal and S. R. Bhattacharyya, *J. Nanosci. Nanotechno.*, 2013, **13**, 3983-3989.
26. Y. T. Lu and A. R. Barron, *Phys. Chem. Chem. Phys.*, 2013, **15**, 9862-9870.
27. K. Q. Peng, J. J. Hu, Y. J. Yan, Y. Wu, H. Fang, Y. Xu, S. T. Lee and J. Zhu, *Adv. Funct. Mater.*, 2006, **16**, 387-394.
28. C. L. Lee, K. Tsujino, Y. Kanda, S. Ikeda and M. Matsumura, *J. Mater. Chem.*, 2008, **18**, 1015-1020.
29. K. I. Ishibashi, Y. Kimura and M. Niwano, *J. Appl. Phys.*, 2008, **103**, 094507.
30. S. Perraud, S. Poncet, S. Noel, M. Levis, P. Faucherand, E. Rouviere, P. Thony, C. Jaussaud and R. Delsol, *Sol. Energy Mater. Sol. Cells*, 2009, **93**, 1568-1571.

31. J. Oh, H. C. Yuan and H. M. Branz, *Nat Nanotechnol.*, 2012, **7**, 743-748.
32. G. K. Reeves and H. B. Harrison, *IEEE Electron Device Lett.*, 1982, **3**, 111-113.